Journal of the Mechanics and Physics of Solids 92 (2016) 55–71

Contents lists available at ScienceDirect

Journal of the Mechanics and Physics of Solids

journal homepage: www.elsevier.com/locate/jmps

Scaling laws of nanoporous gold under uniaxial compression: Effects of structural disorder on the solid fraction, elastic Poisson's ratio, Young's modulus and yield strength

B. Roschning [a,b,*], N. Huber [a,b]

[a] Institute of Materials Physics and Technology, Hamburg University of Technology, Eißendorfer Straße 42 (M), 21073 Hamburg, Germany
[b] Institute of Materials Research, Materials Mechanics, Helmholtz-Zentrum Geesthacht, Max-Planck-Straße 1, 21502 Geesthacht, Germany

ARTICLE INFO

Article history:
Received 28 August 2015
Received in revised form
30 November 2015
Accepted 16 February 2016
Available online 27 February 2016

Keywords:
Nanoporous gold
Scaling laws
Finite element method
Yield strength
Young's modulus
Poisson's ratio
Mechanical behavior

ABSTRACT

In this work the relationship between the structural disorder and the macroscopic mechanical behavior of nanoporous gold under uniaxial compression was investigated, using the finite element method. A recently proposed model based on a microstructure consisting of four-coordinated spherical nodes interconnected by cylindrical struts, whose node positions are randomly displaced from the lattice points of a diamond cubic lattice, was extended. This was done by including the increased density as result of the introduced structural disorder. Scaling equations for the elastic Poisson's ratio, the Young's modulus and the yield strength were determined as functions of the structural disorder and the solid fraction. The extended model was applied to identify the elastic–plastic behavior of the solid phase of nanoporous gold. It was found, that the elastic Poisson's ratio provides a robust basis for the calibration of the structural disorder. Based on this approach, a systematic study of the size effect on the yield strength was performed and the results were compared to experimental data provided in literature. An excellent agreement with recently published results for polymer infiltrated samples of nanoporous gold with varying ligament size was found.

1. Introduction

Samples of nanoporous gold, made by dealloying, take the form of a monolithic homogenous network structure consisting of nanoscale ligaments with a uniform ligament size between 5 and 500 nm (Erlebacher et al., 2001; Hakamada and Mabuchi, 2007; Li and Sieradzki, 1992; Parida et al., 2006; Weissmüller et al., 2009). The macroscopic samples can be described as porous bodies with a solid fraction around 30% (Erlebacher et al., 2001; Li and Sieradzki, 1992). Current research focuses on the prospective use as functional material for catalysis (Ding and Chen, 2009; Snyder et al., 2010; Wang et al., 2012), actuation (Biener et al., 2009; Kramer et al., 2004) and sensing (Chen et al., 2012) applications. For each of these fields the mechanical properties are of importance. It is noteworthy that the strength of nanoscale objects–such as the ligaments in nanoporous gold–increases systematically with decreasing size (Biener et al., 2006; Volkert and Lilleodden, 2006). Resulting from the well-described manufacturing process, nanoporous gold has been established as a model system

* Corresponding author at: Institute of Materials Physics and Technology, Hamburg University of Technology, Eißendorfer Straße 42 (M), 21073 Hamburg, Germany.
E-mail address: benedikt.roschning@tuhh.de (B. Roschning).

http://dx.doi.org/10.1016/j.jmps.2016.02.018
0022-5096/

for the study of the mechanical properties at the nanoscale. So produced macroscopic samples of several millimeters in size provide access by micro- or macromechanical testing while exploiting the strength of nanoscale objects (Huber et al., 2014; Li and Sieradzki, 1992; Ngô et al., 2015). The crystal lattice of the initially undealloyed lattice survives the dealloying process, leading to a much larger grain than ligament size (Weissmüller et al., 2009). Nanoporous structures with a ligament size in the order of nanometers have an average grain size in the order of microns, meaning a single grain consists of billions of ligaments (Jin et al., 2009).

Porous materials can be characterized by their porosity, thus by the solid fraction $\varphi = \rho/\rho_s$, where ρ denotes the density of the porous material and ρ_s the density of the solid phase. The Gibson-Ashby scaling laws for open cell foams (Gibson and Ashby, 1997), which are well established for cell sizes in the micrometer range, are commonly applied to nanoporous metals, providing a relationship between the solid fraction and the mechanical behavior. These scaling laws do not consider specific geometric features and it is assumed, that the geometry of nanoporous gold does not fundamentally differ from the one for macroporous materials (Weissmüller et al., 2009). Therefore, the Gibson-Ashby scaling laws have been adapted to nanoporous gold and are giving a good starting point for the evaluation of the mechanical behavior in terms of the macroscopic Young's modulus E and the macroscopic yield strength σ_y by

$$\frac{E}{E_s} = C_E\,\varphi^2 \tag{1}$$

and

$$\frac{\sigma_y}{\sigma_{ys}} = C_\sigma\,\varphi^{3/2}. \tag{2}$$

In the previous equations the subscript s denotes the material properties of the solid phase and C_E and C_σ are constants determined by experiments.

The first experimental studies of the mechanical behavior of nanoporous gold used nanoindentation or micropillar compression. Their results, as summarized in (Hodge et al., 2007; Weissmüller et al., 2009; Yang and Li, 2008), were consistent with the Gibson-Ashby equations for the variation of strength with solid fraction and with a power-law relation between strength and structure size (Greer et al., 2005; Uchic et al., 2004; Volkert et al., 2006). Further work combining the analysis based on the Gibson-Ashby model with experimental investigations on nanoporous metals suggested incorporation of a Hall–Petch-type relationship between the average yield strength and the average ligament diameter (Hodge et al., 2007).

Recently, studies using atomistic simulations have confirmed the general trends of the previous experiments, while suggesting corrections to the scaling law (Sun et al., 2013) and pointing towards deviations (Farkas et al., 2013) between the plastic behavior in compressive and tensile direction. Yet being able to deform macroscopic samples of nanoporous gold to large compressive strains, further investigations led to inconsistencies to previous results (Huber et al., 2014; Jin et al., 2009; Wang et al., 2015), indicating that the material's coupling behavior between the solid phase and the macroscopic mechanical response is still not fully clarified.

2. Scaling laws for a unit cell

Huber et al. concluded in (Huber et al., 2014) that the scaling of nanoporous gold depends on the complexity of the unit cell, which also includes the degree of randomization. The scaling laws derived from a simple ball-and-stick model and the major results of a subsequent finite element study for a randomized structure, presented in (Huber et al., 2014), will be briefly summarized in the following sections.

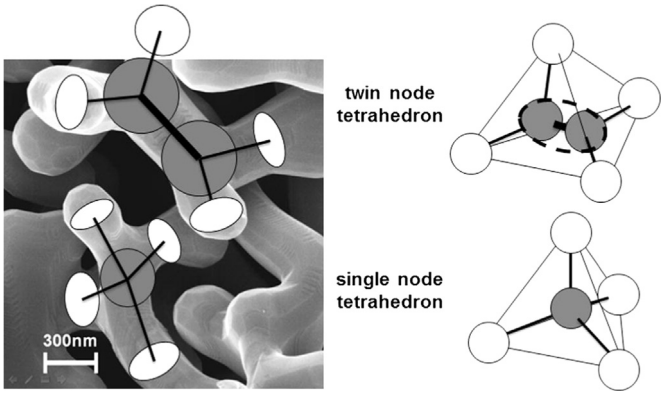

Fig. 1. Scanning electron micrograph and simplification of a three dimensional interconnected nanoporous gold structure to tetrahedral building blocks (from Huber et al., 2014).

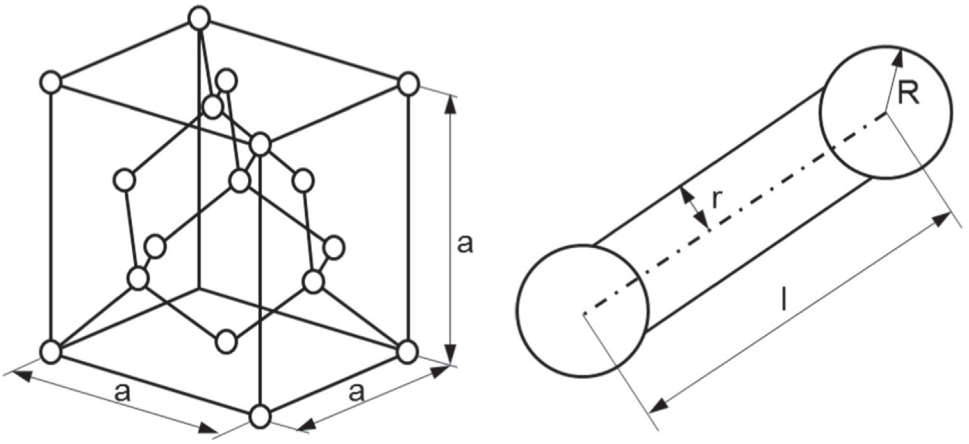

Fig. 2. Diamond cubic unit cell (left) and detailed view of a single ligament attached to spherical nodes (right).

2.1. Perfect diamond lattice

Micrographs of nanoporous gold (Fig. 1) show a network structure of ligaments connected in nodes. Based on these micrographs, the simplest appropriate structure, a periodic array of tetragonal cells composed of cylindrical beams (ligaments) and spheres (nodes connecting the ligaments), was assumed. The resulting representative structure - diamond cubic - as shown in Fig. 2, is characterized by the unit cell size, a, the nodal spacing, l, the ligament radius, r, and the nodal radius, R. Assuming touching of the ligaments on the nodal surface, the ratio between node and ligament radius is given by $R/r=\sqrt{3/2}$. If the condition is formulated that the ligaments do not touch at the nodal surface, the ratio can be written more general as $R = rc_R\sqrt{3/2}$, with $c_R > 1$.

The solid fraction φ, defined by the described choice of unit cell geometry forms the basis of the model:

$$\varphi = \frac{3\sqrt{3}}{4}\pi\left(\frac{r}{l}\right)^3\left[\frac{l}{r} + \left(2c_R^2 - \frac{4}{3}\right)\sqrt{\frac{3}{2}c_R^2 - 1} - \sqrt{\frac{3}{2}}c_R^3\right]. \tag{3}$$

For the common assumption of thin beams, neglecting the nodal volume, Eq. (3) simplifies to $\varphi = 3\sqrt{(3)}/4\pi(r/l)^2$. As reported in (Huber et al., 2014), a solid fraction of $\varphi = 0.26$ leads to a relative deviation between the respective solid fractions of 22%.

For the given unit cell geometry the stiffness was derived, using the Euler–Bernoulli theory, resulting in a relationship for the macroscopic effective modulus in the form:

$$\frac{E}{E_S} = c_E\left(\frac{r}{l}\right)^4,\ c_E = \frac{9\sqrt{3}}{8}\pi \approx 6.\,1. \tag{4}$$

Inserting the simplified equation for the volume fraction, it can be seen that the relation agrees in the power to the Gibson-Ashby scaling equation. The pre-factor can be calculated to 0.37, which is roughly half the value of 2/3, given by Gibson and Ashby, meaning that the model of the diamond lattice is about a factor 2 more compliant than the periodic models of open cell solids presented in (Gibson and Ashby, 1997; Roberts and Garboczi, 2002). The presence of nodes with a finite extension was neglected, because the elastic strain field penetrates well into the node and therefore already contributes to the compliance of the unit cell (Huber et al., 2014).

For thicker ligaments the shear deformation can no longer be neglected and the effect of the Timoshenko beam theory, included in the finite element beam model, requires a correction. The suggested equation

$$\frac{E}{E_S} = c_E\left(\frac{r}{l}\right)^4\left(1+\frac{r}{l}\right)^{-4}\left(1+\frac{r}{l}\right)^2,\ c_E=5.\,8 \tag{5}$$

incorporates a shift in the power of the scaling law from 4 to 2, for r/l approaching large values.

For the macroscopic yield strength of the diamond unit cell, a scaling law was derived assuming plastic yielding in the outer fiber of the beam at the connection to the node, as

$$\frac{\sigma_y}{\sigma_{yS}} = c_{\sigma_y}\left(\frac{r}{l}\right)^3. \tag{6}$$

The nodal extension, as illustrated in Fig. 3, leads to a reduction of the actual lever length and the shortened lever will reduce the actual bending moment. Because the shortening of the lever neither occurs in the scaling law of the yield

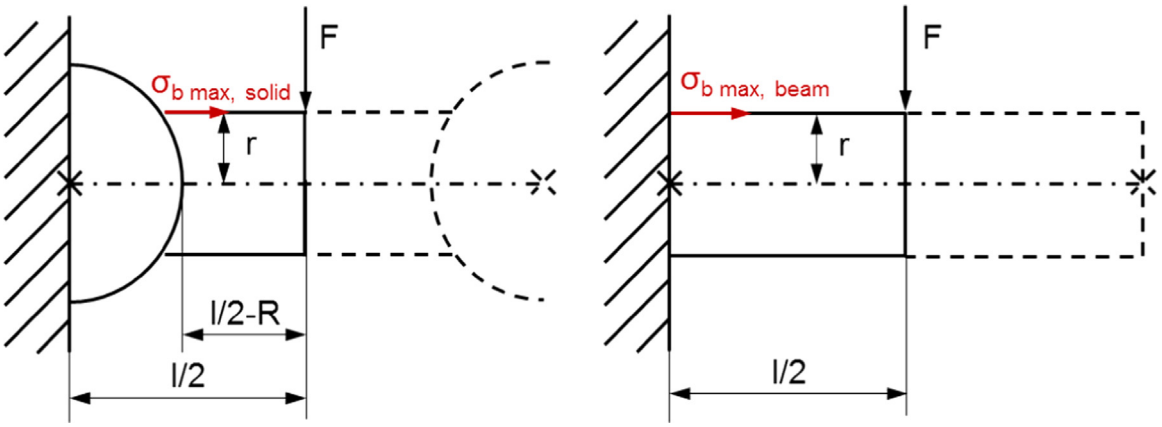

Fig. 3. Ligament with nodal extension (left) and ligament as modeled without nodal extension (right).

strength nor in the finite element model, the result is an overestimation of the bending stress and therefore an overestimation of the compliance in the finite element model. Taking the nodal extension into account, the correction for the effect of the nodal extension was considered in the form

$$\frac{\sigma_y}{\sigma_{yS}} = c_{\sigma_y}\left(\frac{r}{l}\right)^3\left(1-\sqrt{6}\,c_R\frac{r}{l}\right)^{-1},\ \frac{r}{l} < \frac{1}{\sqrt{6}\,c_R}. \tag{7}$$

After creating finite element models in Abaqus, the results for a solid diamond cubic structure modeled by C3D6 triangular prism elements were compared to the results of a beam structure modeled by B31 elements. As already shown in (Huber et al., 2014), the deviations introduced by the simplification of the structure with beam elements can be easily corrected according to Eq. (7), see section 4.2. The simplification reduces the number of elements within a representative volume element of $4\times4\times4$ unit cells from 257760 to 20480 elements. This reduces the calculation time with an elastic–plastic material model from 15 CPU h to 0.5 CPU h. Furthermore, the beam model allows a study of the dependence of the geometry parameter r/l by variation of the ligament radius in the element properties instead of creating a new solid model for each geometry. This considerable increase in efficiency finally allows an extensive variation of parameters as shown in the presented study.

2.2. Randomized structure

Additional to the previous considerations the effect of systematic structural randomization was investigated, using a finite element beam model to have a more realistic interconnected structure. The connecting nodes are shifted randomly by an amplitude A. The shift along each coordinate direction u_i is an independent random number in the interval $-A \le u_i/a \le +A$, obtained from an equal distribution. During the nodal shifting, the elements representing the ligaments follow the nodal displacement by elastic deformation. The resulting geometry provides the structural information for a distorted model with $A > 0$.

The numerical results for degrees of randomization up to $A = 0.4$ can be represented by a fit function as given by Eqs. (8–11), with a_{ij} as fit parameters.

$$\frac{E(A)}{E(A=0)} = A_1(A) + \left[A_2(A) - A_1(A)\right]\left[1 + 10^{\left(0.4-\frac{r}{l}\right)A_p(A)}\right]^{-1}, \tag{8}$$

$$A_1(A) = 1 + a_{11}A + a_{12}A^2 + a_{13}A^3, \tag{9}$$

$$A_2(A) = 1 + a_{21}A + a_{22}A^2 + a_{23}A^3, \tag{10}$$

$$A_p(A) = a_{p1} + a_{p2}e^{-\left(\frac{A}{a_{p3}}\right)^2}. \tag{11}$$

Within the range of $0.01 \le r/l \le 1$ the dependence of the yield strength on the parameter A was determined in the same manner by finite element simulations and approximated by the fit function

$$\frac{\sigma_y(A)}{\sigma_y(A=0)} = 1 - A\left[b_1 + b_2\left(\frac{r}{l}\right)^{-b_3}\right], \tag{12}$$

with b_i being fit parameters.

It was concluded in (Huber et al., 2014) that the variation of the macroscopic Young's modulus with the solid fraction is

well approximated by the Gibson-Ashby scaling law, given in Eq. (1). Even for structures with randomized nodal positions. Aside from the adjusted leading constant, it was found that this relation is no longer valid as soon as the unit cell is deformed in elastic–plastic compression. Concerning the yield strength, the Gibson-Ashby scaling does not apply according to Eq. (12), which is a consequence of the reduced lever length due to the nodal extension.

Recently, Pia and Delogu investigated the effect of the ligament's thickness variation along their length (Pia and Delogu, 2015b) as well as the effect of the statistical distribution of the ligament length to thickness ratio on the yield strength (Pia and Delogu, 2015a), using Timoshenko beam theory. A major outcome of their work was a shift of the elastic deformation from the ligaments' ends towards their thinner center. While a variation of the ligament length to thickness ratio is considered in (Huber et al., 2014), the thickness variation along the ligament length is incorporated phenomenological in form of the geometry parameter c_R describing the nodal extension. By tuning c_R a reduction of the lever available for bending, thus a shift of deformation towards the ligament center can be achieved.

3. Further development of the model

The presented finite element beam model is based on the approach described in (Huber et al., 2014). The representative volume element (RVE) consists of $4 \times 4 \times 4$ unit cells, whereas the model was created dimensionless. Because the unit cell size a was fixed at the numerical value 1 (one), the lengths and forces in the model are always in relation to the actual unit cell size. If desired, the model can be scaled to any ligament size based on geometric similarity. This approach works without restriction of generality, as long as the constitutive law does not include any length scales, such as gradient theory for capturing size effects. Each ligament is modeled in Abaqus by a sequence of 20 individual B31 beam elements (Dassault Systèmes, 2014). The beam elements allow transverse shear strain, leading to Timoshenko beam theory, which is generally considered useful for thicker beams, whose shear flexibility may be important (Dassault Systèmes, 2014). Such a beam model allows studying the dependency of the geometry parameter r/l via variation of the ligament radius by changing the element properties. Furthermore, it is possible to modify the individual ligament length by shifting each connecting node by a given random displacement. A more realistic interconnected structure according to Fig. 4 is obtained by the procedure summarized in section 2.2.

In this section, the influence of the boundary conditions will be investigated and the calculation of the solid fraction for the randomized RVE will be improved. The latter is affected by the randomization in two aspects: (i) the distortion of the RVE planes makes a correct volume calculation difficult, and (ii) the change in ligament length due to the nodal shifting increases the volume of the solid fraction. Because the solid fraction is the most important structural parameter in the scaling laws, both aspects are of high relevance for all subsequent steps.

3.1. Boundary conditions

The boundary conditions were chosen in (Huber et al., 2014) consistent to a solid model with symmetry conditions applied to the nodes in the planes $x = 0$, $y = 0$, and $z = 0$. The load was applied as homogeneous displacement of all nodes on the top side of the RVE. To capture the boundary conditions of a uniaxial compression experiment, all nodes on the remaining faces are free to move. A comparison of the macroscopic response of different RVEs consisting of $1 \times 1 \times 1$, $2 \times 2 \times 2$, and $4 \times 4 \times 4$ unit cells showed that the macroscopic properties converge within a few percent accuracy, if the results are averaged from a sufficient number of realizations. An RVE size consisting of $4 \times 4 \times 4$ unit cells with 10 random

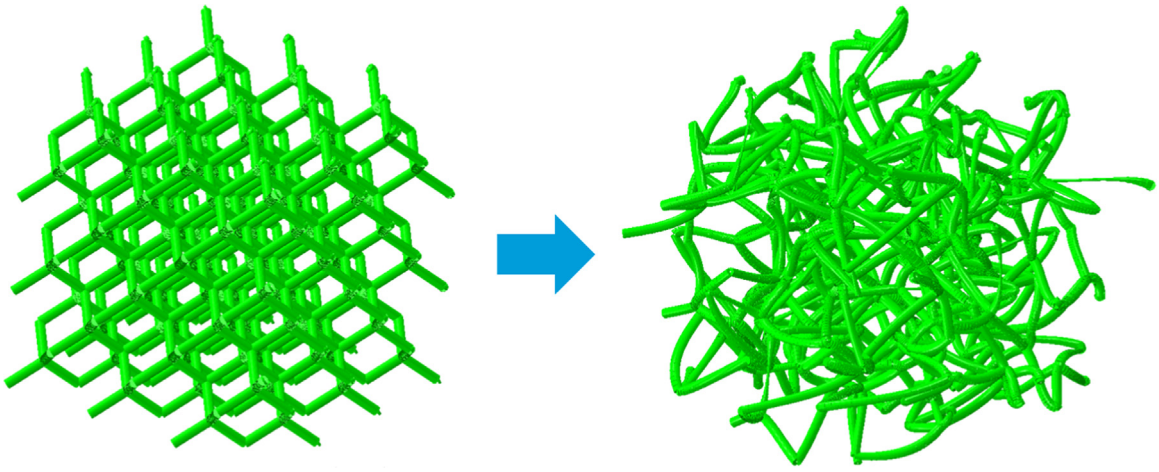

Fig. 4. Randomization of a diamond structure by randomly shifting the connecting nodes of the ligaments. The ligaments follow the connecting nodes by elastic deformation.

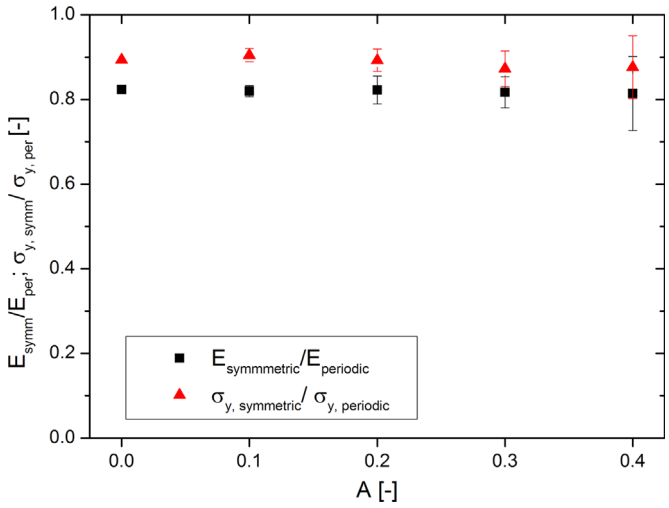

Fig. 5. Effect of the boundary conditions on the macroscopic behavior of the RVE in terms of Young's modulus and yield strength.

realizations is found sufficient with respect to accuracy and computation time and is used consistently for all following investigations.

To investigate possible effects of the boundary conditions on the macroscopic behavior of the RVE, the model with symmetric boundary conditions was compared to a model with periodic ones corresponding to larger specimens as used in experiments. To enable the coupled pairs of nodes to be on opposite faces of the RVE, the initially opposite nodes are shifted by the same random value. In contrast to a solid model, where only displacements are defined as periodic, the rotational degrees of freedom also need to be considered (Zhu et al., 2000). Therefore, a pair of coupled nodes has the same rotations in all directions. To avoid an unrealistic clamping in lateral direction, the normal displacements of the nodal pairs on the side planes are forced to take the same magnitude in opposite sign. All simulations are performed for a constant ratio of $r/l = 0.162$ and the following material parameters for the solid fraction $E_S = 81$ GPa, $\nu_S = 0.42$ and $\sigma_{yS} = 500MPa$, taken from (Huber et al., 2014). Values for the calculated ligament modulus and yield strength as function of the ligament diameter can be found in (Weissmüller et al., 2009). The material parameters in this work correspond roughly to a ligament size of ~100 nm. The results for the two sets of boundary conditions are compared in Fig. 5, presenting both, the Young's modulus and yield strength of the RVE for symmetric boundary conditions normalized by the values for periodic boundary conditions. All data are plotted in dependence of the amplitude of disorder, A. It can be seen that the Young's modulus of the RVE with symmetric boundary conditions is ~82% of the Young's modulus of the RVE with periodic ones, whereas the yield strength is ~89%, respectively. The relative error increases for increasing disorder up to 8.8% for the Young's modulus and to 7.4% for the yield strength, due to the fact that the absolute error is roughly the same for each individual value of A, whereas the mean decreases. Compared to other effects (see the following sections) and experimental issues (see Section 4), the effect of the chosen boundary conditions is well within several other uncertainties.

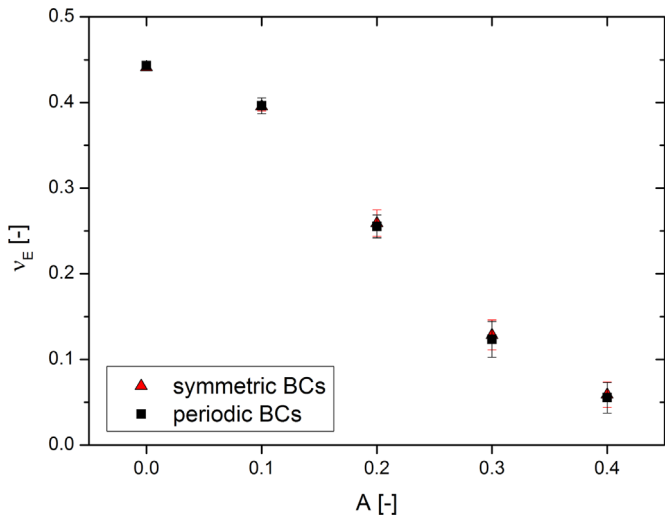

Fig. 6. Effect of the boundary conditions on the macroscopic behavior of the RVE in terms of the elastic Poisson's ratio.

Additionally the elastic Poisson's ratios ν_E for the two sets of boundary conditions were compared, as shown in Fig. 6. As qualitatively demonstrated in (Huber et al., 2014), it can be seen that the elastic Poisson's ratio is strongly dependent on the randomization parameter A. Furthermore, it is not sensitive to the different boundary conditions.

The increased stiffness and strength for periodic boundary conditions is caused by two mechanisms. Microscopically, periodic boundary conditions constrain the displacements and rotations of nodal pairs on opposite sides. Although, nodes may move independently from their neighbors, e.g. out of plane, the corresponding node on the opposite plane feels a resistance against its displacement through the elastic distortion of its neighborhood. This leads in average to more or less plain deformation of all nodes on an RVE surface while in addition the rotation of the node is restricted. Macroscopically, the model with periodic boundary conditions represents a sample with infinite extension perpendicular to the load direction, whereas the extension parallel to the load direction is finite. It can be compared to compression of a film, which is an unfavorable geometry to determine material parameters by normal compression loading. These two mechanisms lead to an overestimation of the mechanical response for periodic boundary conditions, as shown in Fig. 5.

Experiments on nanoporous gold are usually performed on cubic or cylindrical samples with finite dimensions (Jin et al., 2009; Lührs et al., 2016; Volkert and Lilleodden, 2006; Wang et al., 2015; Wang and Weissmüller, 2013). Taking the previous considerations into account, symmetric boundary conditions are seen as the better representation of the macroscopic geometry and are used for further evaluation.

3.2. RVE boundary

An uncertainty in the approach presented in Section 2.2 is that the distorted RVE has no defined edges and planes. The random shifting also includes the ligament ends touching the boundaries of the initial cubic RVE. After randomization, the boundaries are strongly distorted, changing the volume of the RVE. A simple solution to overcome this obstacle is to create an initial model larger than the required one and subsequently cutting out the desired geometry. An exemplary mesh of a RVE created by the presented routine is shown in Fig. 7.

The cutting procedure leads to small remaining beam fractions close to the cutting edges, which are not connected to the network structure. Because the remaining fractions lead to additional degrees of freedom within the model, which are not properly constrained, an algorithm was written to delete them. The total length of all deleted ligaments in relation to the total ligament length within the RVE increases from $0.24 \pm 0.13\%$ for $A = 0.1$ to $2.92 \pm 0.59\%$ for $A = 0.4$.

3.3. Effect of randomized nodal positions

To investigate the effect of the parameter A on the elastic Poisson's ratio, the Young's modulus and the yield strength of the RVE, a finite element study was performed with the following material parameters, $E_S = 81$ GPa, $\nu = 0.42$. For the elastic–plastic

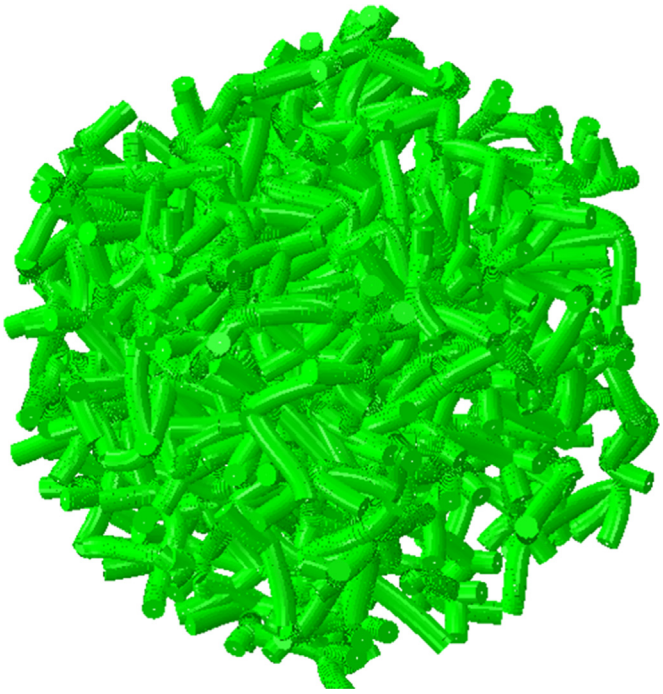

Fig. 7. Example of a $4 \times 4 \times 4$ RVE for $\boldsymbol{A} = 0.4$ after cutting from a significantly larger randomized structure.

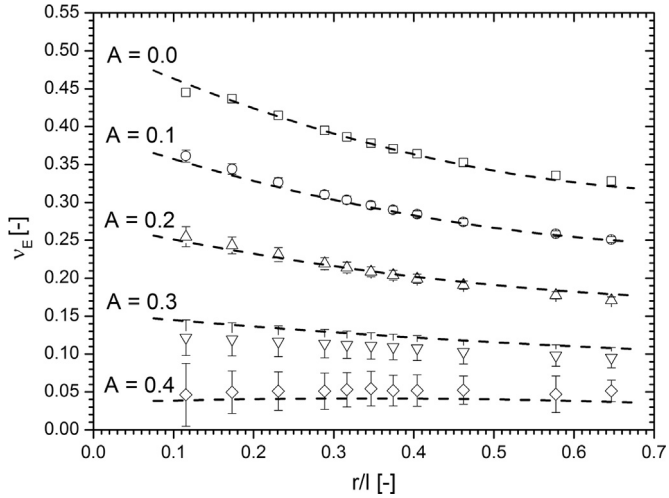

Fig. 8. Effect of the random nodal positions on the Poisson's ratio in dependence of ***A*** and ***r*/*l***. The markers correspond to the numerical results from the finite element beam model, the dashed curves represent the fit functions.

material behavior isotropic plasticity without work hardening was used. The yield strength was set to $\sigma_y = 500$ MPa. The interval of the investigated r/l ratio was determined according to Eq. (3) for solid fractions in the range $0.05 \leq \varphi \leq 0.99$ to $0.1 \leq r/l \leq 0.65$. A structure with a solid fraction around 30%, such as nanoporous gold, falls within the scope of investigation. The effect of the geometry parameters r/l and A on the relevant mechanical properties was determined from 10 different randomized realizations of the RVE. A visual inspection of the randomized structures up to $A = 0.4$ showed no intersections of beam elements. Independent of that, it would have no consequences on the mechanical behavior, because contact between beam elements is not implemented in the model.

3.3.1. *Effect on the elastic Poisson's ratio*

The effect of the parameter A on the elastic Poisson's ratio of the RVE is shown in Fig. 8. The numerical results can be represented as a fit function given by Eqs. (13–16), added to the plot as dashed lines (Table 1).

$$\nu_E = B_1(A) + B_2(A)\frac{r}{l} + B_2(A)\frac{r^2}{l}, \tag{13}$$

$$B_1(A) = b_{11} + b_{12}A, \tag{14}$$

$$B_2(A) = b_{21} + b_{22}A, \tag{15}$$

$$B_3(A) = b_{31} + b_{32}A. \tag{16}$$

In Fig. 8 it can be seen that for increasing randomization A the effect of the solid fraction, represented by r/l, on the elastic Poisson's ratio is decreasing. In other words, for large values of A the elastic Poisson's ratio becomes nearly independent of the ligament's aspect ratio and is heavily dependent on the structural disorder. However, for more ordered structures ($A \leq 0.2$) the elastic Poisson's ratio shows a significant decrease for increasing ligament thickness, which is due a change of the ligament's deformation mechanism. The deformation of thin ligament is mainly due to bending, whereas thick ligaments mainly undergo axial deformations. Because the deformation mechanism of the ligaments also depends on their load direction, thus on their orientation in space, this effect is less pronounced for more irregular structures.

3.3.2. *Effect on modulus*

The influence of the parameter A on the Young's modulus of the RVE for different r/l ratios is presented by the markers in Fig. 9. The numerical results can be represented by a fit function as given in Eqs. (17–19), added to the plot as dashed lines (Table 2).

Table 1
Parameters for the fit functions B_1, B_2 and B_3.

Eq. (14)	$b_{11} = 0.50846$	$b_{12} = -1.18144$
Eq. (15)	$b_{21} = -0.48075$	$b_{22} = 1.28409$
Eq. (16)	$b_{31} = 0.29554$	$b_{32} = -0.8599$

Table 2
Parameters for the fit functions A_1 and A_2.

Eq. (18)	a_{11}= − 0.83557	a_{12}= − 2.3265
Eq. (19)	a_{21}=0.17248	a_{22}=1.52856

Table 3
Parameters for the fit functions A_3 and A_4.

Eq. (21)	b_{11}= − 0.65475	b_{12}= − 1.2685
Eq. (22)	b_{21}= − 0.08715	b_{22}=0.89894

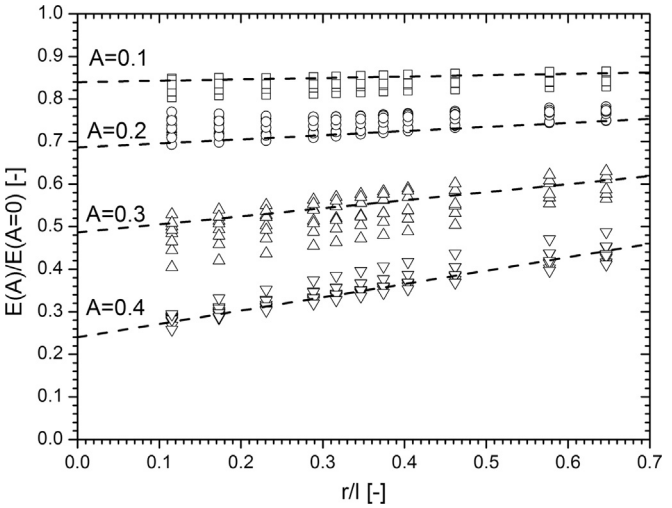

Fig. 9. Effect of the random nodal positions on the modulus in dependence of $\boldsymbol{A}$ and $\boldsymbol{r/l}$. The markers correspond to the numerical results from the finite element beam model, the dashed curves represent the fit functions.

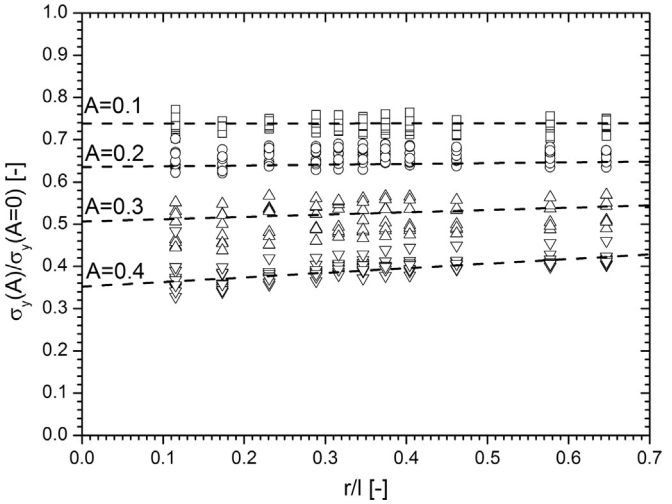

Fig. 10. Effect of the random nodal position on the yield strength in dependence of $\boldsymbol{A}$ and $\boldsymbol{r/l}$. The markers correspond to the numerical results from the finite element beam model, the dashed curves represent the fit functions.

$$\frac{E(A)}{E(A=0)} = A_1(A) + A_2(A)\frac{r}{l}, \tag{17}$$

$$A_1(A) = 0.94636 + a_{11}A + a_{12}A^2, \tag{18}$$

$$A_2(A) = a_{21}A + a_{22}A^2. \tag{19}$$

3.3.3. Effect on yield strength

The influence of the parameter A on the yield strength of the RVE for different r/l ratios is presented by the markers in Fig. 10. The numerical results can be represented by a fit function as given in Eqs. (20–22), added to the plot as dashed lines (Table 3).

$$\frac{\sigma(A)}{\sigma(A=0)} = A_3(A) + A_4(A)\frac{r}{l}, \tag{20}$$

$$A_3(A) = 0.81683 + b_{11}A + b_{12}A^2, \tag{21}$$

$$A_4(A) = b_{21}A + b_{22}A^2. \tag{22}$$

A comparison of the fit functions Eqs. (17–22) to the fit functions Eqs. (8–12) as derived in (Huber et al., 2014) yields comparable slopes in the considered r/l range, whereas the $E(A)/E(A=0)$ resp. the $\sigma_y(A)/\sigma_y(A=0)$ intercept decreases. For thin beams with $r/l < 0.1$, which are not considered in this work, the slope rapidly decreases and the curves show a plateau (Huber et al., 2014). Therefore, the presented fit functions are only valid within the investigated range of r/l.

3.4. Solid fraction

Eq. (3) was derived for the undistorted diamond lattice. The distortion of the RVE changes the ligament length, the solid volume in the RVE, and finally the solid fraction. This effect was not discussed in (Huber et al., 2014). Using a RVE with plain boundaries, as presented in Fig. 7, its volume is now well-defined and the solid fraction can be precisely calculated.

The calculation of the solid fraction according to Eq. (3) is exact for the perfect diamond lattice. Overlapping volumes at the connecting nodes are eliminated by considering the radius of the spherical node in form of the parameter c_R. Because the ligament ends are connected in these nodes, the coupled beam elements share all rotational degrees of freedom. Thus, the distortion has only little effect on the local geometry around the nodes and it is sufficient to consider the change of the accumulated ligament length as basis for the calculation of the effect of the randomization on the solid fraction in the RVE.

The total ligament length $l_{tot}(A) = \sum l_i$ in the distorted structure is calculated and related to the total ligament length in the perfect diamond lattice: $l_{tot}(A=0) = 4^3 \cdot 16 \cdot \frac{\sqrt{3}}{4} a = 443.41a$. The increase in ligament length can be expressed as $\lambda(A) := l_{tot}(A)/l_{tot}(A=0)$. The results of 10 realizations for $0 \le A \le 0.4$ are presented in Fig. 11 including the fit function (solid curve):

$$\lambda(A) = 1 + 0.15A + 2.91A^2. \tag{23}$$

The effect of the randomization on the ligament length for $A < 0.16$ is below 10%. However, for larger values of A the effect is considerable. For example for $A = 0.4$, as used in (Huber et al., 2014), the obtained ratio is $\lambda(A) = 1.52$, i.e. the ligament length in the structure is 52% larger than assumed. This effect is significant and needs to be considered in the calculation of the solid fraction.

Because the randomization affects only the ligament length and not the nodal volume, the solid fraction is not strictly increasing linear with λ. Considering the derivation of Eq. (3) in (Huber et al., 2014), the first term l/r inside the square bracket represents the contribution of the ligament length to the solid volume. Multiplying this term with $\lambda(A)$, the increased ligament length can be incorporated:

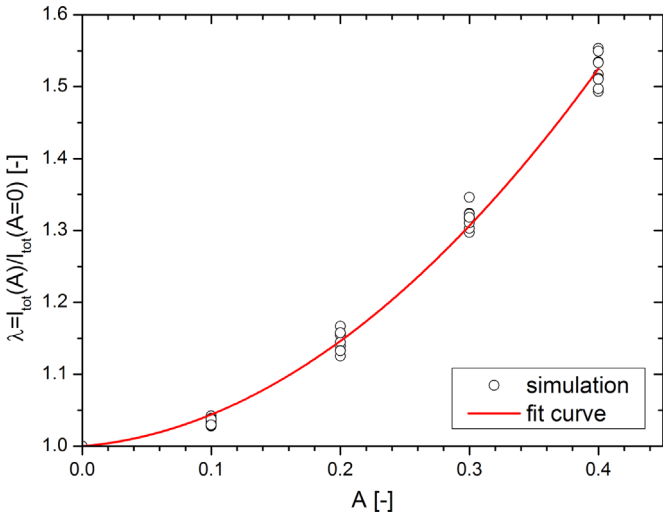

Fig. 11. Effect of ***A*** on the total ligament length. The markers represent 10 realizations for constant randomization; the solid curve represents the fit of all results as function of ***A***.

$$\varphi_{dist} = \frac{3\sqrt{3}}{4}\pi\left(\frac{r}{l}\right)^3\left[\frac{l}{r}\lambda(A) + \left(2c_R^2 - \frac{4}{3}\right)\sqrt{\frac{3}{2}c_R^2 - 1} - \sqrt{\frac{3}{2}}c_R^3\right]. \tag{24}$$

If Eq. (3) is used providing the corrected ratio $r/(l\cdot\lambda(A))$ instead of r/l, the resulting solid fraction must be multiplied by the factor $\lambda^3(A)$ to compensate the influence of the leading constant $(r/l)^3$:

$$\varphi_{dist} = \varphi\left(\frac{r}{l\cdot\lambda(A)}, c_R\right)\cdot\lambda^3(A). \tag{25}$$

The solid fraction is crucial for the interpretation of the mechanical properties from experimental results. It is provided throughout literature along with all types of mechanical tests. With the approach proposed in (Huber et al., 2014), the solid fraction needs to be translated into the geometry parameter r/l for further analysis. This can be easily done by numerical iteration of Eq. (25) with the given geometry parameters c_R and A.

To estimate the effect of $\lambda(A)$ on the mechanical properties, thin beams are assumed, for which a dependency in the form $\varphi_{dist} \sim (r/l(A=0))^2\cdot\lambda(A)$ is obtained. With this consideration the scaling laws (Eqs. (4) and (6)) result in

$$\frac{E}{E_S} = c_E\left(\frac{r}{l(\mathrm{A}=0)}\right)^4 \sim \left(\frac{\varphi_{dist}}{\lambda(A)}\right)^2, \tag{26}$$

$$\frac{\sigma_y}{\sigma_{yS}} = c_{\sigma_y}\left(\frac{r}{l(\mathrm{A}=0)}\right)^3 \sim \left(\frac{\varphi_{dist}}{\lambda(A)}\right)^{3/2}. \tag{27}$$

If the macroscopic modulus and yield strength are measured, the effect of $\lambda(A)$ on the properties of the solid phase can be estimated by

$$E_S \sim \left(\frac{\lambda(A)}{\varphi_{dist}}\right)^2 E, \frac{E_S(A)}{E_S(A{=}0)} \sim \lambda^2(A), \tag{28}$$

$$\sigma_{yS} \sim \left(\frac{\lambda(A)}{\varphi_{dist}}\right)^{3/2} \sigma_y, \frac{\sigma_{yS}(A)}{\sigma_{yS}(A{=}0)} \sim \lambda^{3/2}(A). \tag{29}$$

The resulting behavior of Eqs. (28) and (29) is plotted in Fig. 12. Taking the effect of the increased solid fraction due to the increased randomization into account, it can be seen that the determined values of the Young's modulus and the yield strength are considerably higher than without the effect. For $A = 0.4$ the estimated effect on the determined Young's modulus and the yield strength of the solid phase takes factors of 2.3 and 1.9, respectively. However, because the parameter A itself was determined in (Huber et al., 2014) by calibration of the model's response to a measured macroscopic modulus, it can be expected that this parameter will also change by consideration of the corrected solid fraction in form of Eq. (25) in the analysis of experimental results.

The nodal shifting changes (i) the structural irregularity (ii) and the solid fraction. Thus, structures with the same solid fraction could be different with each other. A totally ordered structure with thick ligaments could have the same solid fraction as a highly randomized structure with thin ligaments. However, in Fig. 13 it can be seen that the solid fraction is

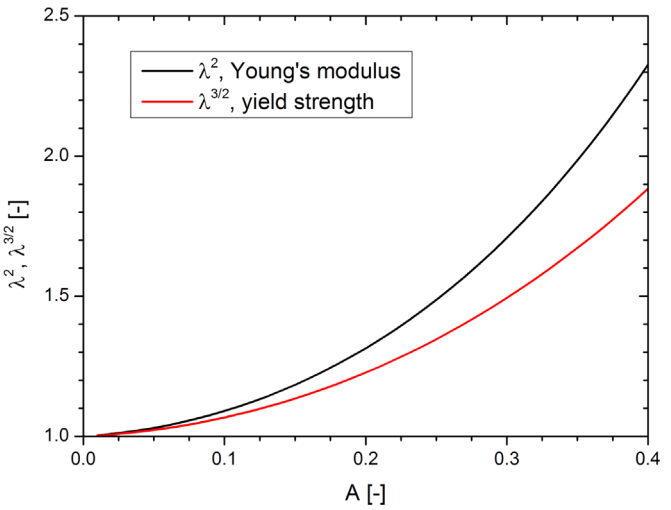

Fig. 12. Estimation of the effect of the increased solid fraction as result of the increased randomization on the determined mechanical properties.

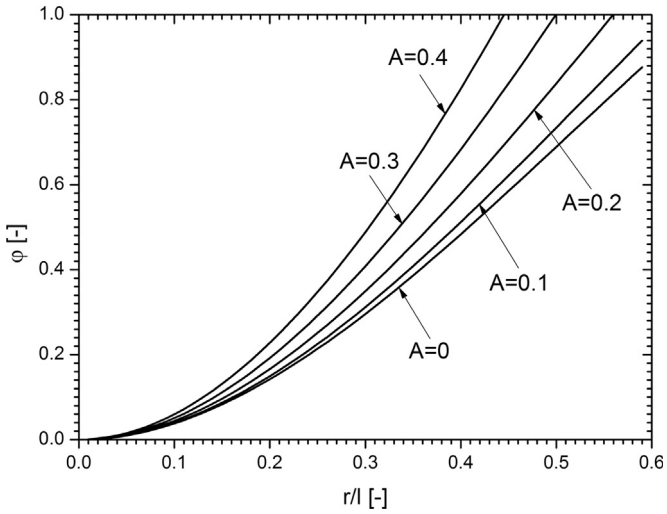

Fig. 13. Solid fraction in dependence of the geometry parameter r/l and A.

uniquely determined by r/l for a given A, as derived from Eq. (25), and vice versa. Translating the solid fraction to r/l, the value of the randomization parameter A is required. As it will be shown in section 4.1, this parameter can be independently determined from the elastic Poisson's ratio.

The equations in section 3.3 quantify the effect of the structural disorder on the macroscopic response of the structure. The result is a superposition of lowering the stiffness and strength due to the structural disorder and increasing them due to an increased relative density. Considering Fig. 9 and Fig. 10 it can be seen, that at a fixed r/l ratio the stiffness and strength are decreasing with increasing disorder. From this observation it can be concluded that the effect of the structural disorder dominates the effect of the densification. The Poisson's ratio is rather influenced by the structural irregularity than by the densification (Gibson and Ashby, 1997).

4. Application to experiments

In the following section, the extended scaling laws will be applied to experimental data presented in (Lührs et al., 2016) and (Huber et al., 2014). This allows a determination of the parameter A and an estimation of the corresponding yield strength. In a subsequent step the approach will be applied to recent results by Wang et al. (Wang et al., 2015) allowing an investigation of the size effect on the yield strength.

4.1. Calibration of the randomization parameter A

Nanoporous gold is characterized by almost immediate plastic deformation and a drastic increase of the macroscopic Young's modulus by about one order of magnitude during ongoing deformation (Huber et al., 2014; Mameka et al., 2014). Thus, the absolute value of the Young's modulus depends strongly on the selected relevant strain range. In (Lührs et al., 2016) it was shown that the elastic Poisson's ratio is independent of the ligament size and not sensitive to strain changes which makes its experimental determination considerably more reliable. As shown in the present work, the elastic Poisson's ratio is strongly dependent on structural changes (Fig. 8) and independent to any possible influences of the boundaries (Fig. 6). With the previous considerations, it is evident that the elastic Poisson's ratio provides a much more robust basis for the calibration of the randomization parameter A than the Young's modulus. ν_E and φ were obtained from experimental

Table 4
Elastic Poisson's ratio, corresponding solid fraction obtained from literature (Balk et al., 2009; Lührs et al., 2016; Sun et al., 2013) and corresponding randomization parameter A obtained by numerically solving Eqs. (3), (13–16), (23) and (25).

Ref.	φ [−]	L [nm]	ν_E [−]	A
Lührs et al. (2016)	0.25	50	0.205	0.210
Lührs et al. (2016)	0.27	120	0.165	0.253
Lührs et al. (2016)	0.28	180	0.200	0.212
Balk et al. (2009)	0.3	20–35	0.175	0.239
Sun et al. (2013)	0.28	40	0.18	0.233
				0.229 ± 0.021

Table 5
Geometry parameters of the beam model for given values of $A = 0.23$, $\varphi = 0.26$, and $c_R = 1.1$ and the predicted scaling of the mechanical properties.

A [−]	$\frac{r}{l}$ [−]	$\frac{E(A)}{E_S}$ [−]	$\frac{\sigma_y(A)}{\sigma_{yS}}$ [−]	ν_E [−]
0.23	0.249	$9.37 \cdot 10^{-3}$	$5.64 \cdot 10^{-2}$	0.184

results (Balk et al., 2009; Lührs et al., 2016; Sun et al., 2015) and A was determined as a function of φ and ν_E by numerically solving Eqs. (3), (13–16), (23) and (25) with an error in the solid fraction φ_{dist} below $1 \cdot 10^{-4}$. Table 4 contains the solid fraction, the elastic Poisson's ratio and the corresponding value of A. Combining the presented data results in an average value of $A = 0.23 \pm 0.02$, which describes the elastic Poisson's ratio independent of the ligament size, $L = 2r$, which ranges from 20 nm to 180 nm.

A visual inspection of the randomized structures with the calculated value of $A = 0.23$ showed no intersections of beam elements. For r/l ratios larger than 0.46 the overlap of the ligaments in regions away from the connecting nodes becomes frequent, resulting in additional contact and a reduced solid fraction. This effect would not be captured by the FEM model. As shown in Section 4.2, the r/l ratio for the investigated samples with a volume fraction of ∼30%, is ∼0.27 which is sufficiently below the critical limit.

To verify the determined value of $A = 0.23$, Eqs. (3), (23) and (25) are numerically solved with an error in the solid fraction φ_{dist} below $1 \cdot 10^{-4}$, resulting in the ratio of ligament radius to nodal spacing, as given in Table 5. This table also contains the elastic Poisson's ratio and the scaling of the mechanical properties, calculated from Eqs. (5), (17–19) and Eqs. (7), (20–22) for the Young's modulus and the yield strength, respectively.

Assuming $E_S = 81$ GPa, a macroscopic Young's modulus of $E(A) \approx 750$ MPa is obtained. This value is in good agreement the experimental results in (Huber et al., 2014). Taking the experimental macroscopic yield strength of ∼10 MPa from (Huber et al., 2014), a first estimation of the yield strength of the solid phase is obtained to $\sigma_{ys} \approx 180$ MPa. This value exceeds the yield strength of $\sigma_{ys} \approx 67$ MPa determined in (Huber et al., 2014) more than 2.6 times.

In summary, the effect of the modified RVE boundary and the increased solid fraction due to the distortion of the ligaments leads to an increased ligament length by 19%, a reduction of the randomization parameter A by 43% and an increased yield strength by a factor of 2.6. This disproportionately high effect on the yield strength results from the reduced ligament radius, which is necessary to compensate the increased ligament length due to the randomization at a given solid fraction. Although there is a stiffening and strengthening effect due to the decreased randomization, the scaling of the bending stress in the ligaments with $(r/l)^3$ (see Eq. (7)) strongly dominates the mechanical response. The reduction of r/l by simultaneously decreasing the ligament radius r and increasing the ligament length l requires a corresponding increase in yield strength with a power of three. If the macroscopic strength should remain unchanged, slightly thinner beams require a significant increase in yield strength for compensation.

4.2. Investigation of the size effect

Recently Wang et al. investigated the macroscopic compression behavior of nanoporous gold with varying ligament size L, ranging between 15 nm and 150 nm (Wang et al., 2015; Wang and Weissmüller, 2013). The material with a ligament size of 150 nm yields immediately and the yield strength cannot be determined. Only the remaining compression tests with ligament sizes of 15 nm, 20 nm, and 50 nm were analysed. The measured solid fractions were 0.27 for the smaller ligament sizes and 0.3 for the ligament size of 50 nm.

The provided data were obtained from quasi static compression tests without unloading segments. For the following analysis it is reasonable to assume $A = 0.23$, as determined in the previous section, and the applicability of the scaling law for the Young's modulus. With this information the macroscopic modulus can be predicted from Eqs. (5), (17–19) assuming again a value of $E_s = 81$ GPa. The data from (Wang et al., 2015; Wang and Weissmüller, 2013) are summarized in Table 6 together with the resulting geometry parameters and the scaling factors of the mechanical properties for $c_R = 1.1$.

To compare the predicted macroscopic stress-strain response of the RVE with experimental results, the effect of the reduced lever length due to the nodal extension needs to be included in the finite element model. In (Huber et al., 2014) this was done by modification of the r/l-ratio according to Eq. (7), so that the same $\sigma_y(A)/\sigma_{yS}$-ratio for the beam model is achieved

Table 6
Geometry parameters, solid fraction and macroscopic yield strength taken from (Wang et al., 2015; Wang and Weissmüller, 2013) for $A = 0.232$ and $c_R = 1.1$.

L [nm]	r [−]	φ [−]	l [−]	a [−]	$\frac{r}{l}$ [−]	$\frac{r}{a}$ [−]	σ_y [−]
15	7.5	0.27	29.5	68.2	0.254	0.110	24
20	10.0	0.27	39.4	90.9	0.254	0.110	24
50	25.0	0.30	93.0	214.7	0.269	0.116	6

Table 7
Scaling factors and identified mechanical properties for the data given in Table 6.

L [nm]	$\frac{E(A)}{E_S}$ [−]	E [MPa]	$\frac{\sigma_Y(A)}{\sigma_{YS}}$ [−]	$\frac{\sigma_Y(A)}{\sigma_{ys}^r}$ [−]	σ_{ys} [MPa]	σ_{ys}^r [MPa]
15	$1.01\cdot10^{-2}$	818	$6.26\cdot10^{-2}$	$1.98\cdot10^{-2}$	384	1212
20	$1.01\cdot10^{-2}$	818	$6.26\cdot10^{-2}$	$1.98\cdot10^{-2}$	384	1212
50	$1.24\cdot10^{-2}$	1004	$8.54\cdot10^{-2}$	$2.35\cdot10^{-2}$	70	255

as for a 3D structure which considers the nodal extension. The reduced lever length was emulated via enlargement of the ligament radius by the factor $\left(1-\sqrt{6}\,c_R r/l\right)^{-1/3}$. The downside of this approach is a loss of the elastic information, because the reduced lever length does not significantly influence the elastic response of the RVE.

A more convenient way is to increase the yield strength of the solid in the finite element beam model to emulate the increased strength caused by the length reduction of the lever. This can be easily achieved by scaling the yield strength of the solid phase σ_{ys} by Eq. (6) instead of Eq. (7). Rearranging Eqs. (6) and (7) yields

$$\sigma_{ys}^r = \sigma_{ys}\left(1-\sqrt{6}\,c_R\frac{r}{l}\right)^{-1}. \tag{30}$$

The values of σ_{ys}^r and σ_{ys} are added to Table 7, where σ_{ys}^r represents the model input in the finite element model as explained before, while σ_{ys} is the mechanical property determined as yield strength of the solid phase. The following simulations are performed with the ratio of ligament radius to unit cell size, r/a, and, using geometric similarity, a unit cell size of $a = 1$ mm.

After a first iteration with an elastic-ideal plastic material law, the macroscopic yield strength was determined to 21.36 MPa for the ligament sizes of 15 nm and 20 nm and to 6.59 MPa for the ligament size of 50 nm. At the yield point the deviation between the simulations and the experimental results is only ~10%. However, the continuous increase in strength for increasing plastic deformation cannot be captured with ideal plasticity. Following (Huber et al., 2014), a linear isotropic hardening was added to the model. This is supported by recent findings in (Ngô et al., 2015), where it was shown based on MD simulations that even in nanosized ligaments stacking faults and dislocations can be stored and their density significantly increases during plastic deformation. For the implementation of work hardening in the beam elements, the hardening behavior is defined by the work hardening rate $\gamma = d\sigma/d\varepsilon_p$, where σ is the true stress and ε_p the true plastic strain. The results for the adjusted values of the yield strength and the work hardening rate, summarized in Table 8, are plotted in Fig. 14 as true stress versus true plastic strain curves. According to the experiment, the true stress is calculated as the reaction force in load direction divided by the current cross section of the RVE. To determine the current cross section, the averaged normal displacements of the free boundary planes were added to the corresponding initial extension of the RVE.

The results for the yield strength of the solid phase are compared in Fig. 15 to the experimental values from (Wang et al., 2015). There, the yield strength was determined from compression tests of polymer infiltrated nanoporous gold by subtracting the strength contribution of the polymer phase from the macroscopic strength of the composite. This approach avoids the interpretation of mechanical properties using scaling laws and can be considered as an independent experimental access to the yield strength of the nanoporous gold. It can be seen that the results obtained in this work are in the same order of magnitude as the experimental values presented in (Wang et al., 2015). For comparison, the graph also contains additional data from (Jin et al., 2009). In Fig. 15 it can be seen that there is an excellent agreement for the smaller ligament sizes of 15 and 20 nm, as well as for the additional data point from Section 4.1 with a ligament size of 63 nm. In that sense, it appears that the chosen geometry parameter $c_R = 1.1$ describes the mass concentration at the nodes and the resulting shift of bending into the ligament sufficiently.

Only for the ligament size of 50 nm, the determined yield strength is much too low. The obvious difference with respect to the other samples is the solid fraction, which is more than 10% higher. This could be explained, if the nanostructure of this sample is not self-similar with respect to the other samples. This would have implications on the geometry parameters A and c_R, which cannot be solved at this point without further experimental investigations.

In summary it can be said, that the simulation results support the recent findings of smaller yield strengths compared to gold columns or nanowires of comparable sizes (Volkert and Lilleodden, 2006; Wu et al., 2005) and are inconsistent with

Table 8
Yield strength as derived from the scaling law and hardening rule as determined from the fit to the experimental data in (Wang et al., 2015).

L [nm]	σ_{ys}^r [MPa]	σ_{ys} [MPa]	γ
15	1362	430	514
20	1353	427	278
50	200	55	1816

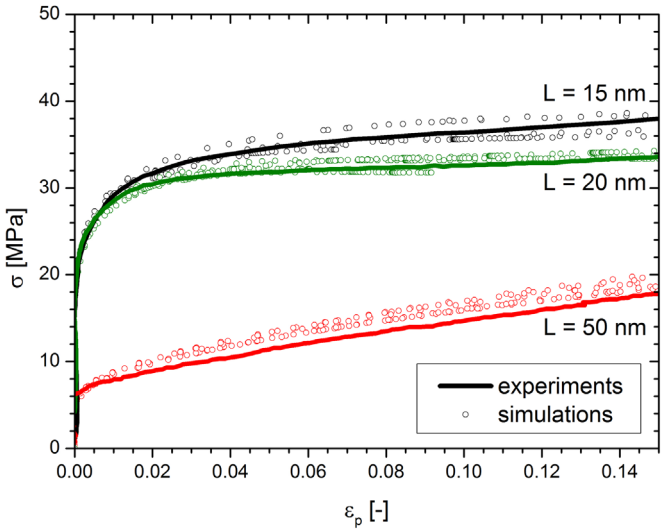

Fig. 14. Graph of true stress vs. true strain, comparing the experimental data for nanoporous gold (solid lines) to the FEM beam model (markers). The ligament sizes, L, indicated by the different colors, were 15 nm, 20 nm and 50 nm. The experimental data were taken from (Wang et al., 2015).

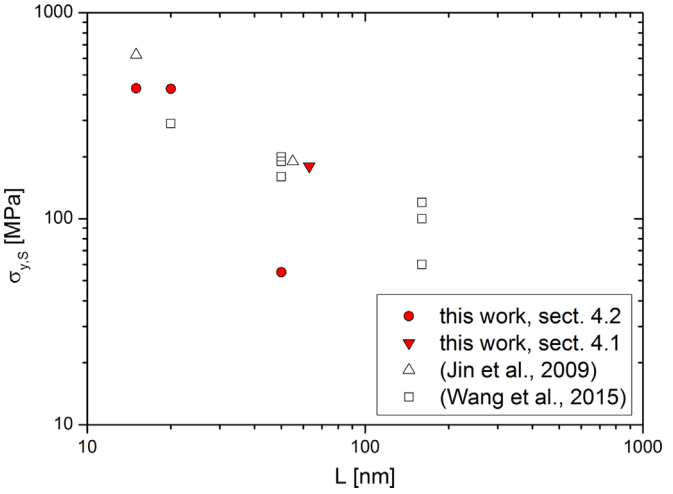

Fig. 15. Yield strength of the solid phase vs. ligament size. Experimental data taken from (Jin et al., 2009; Wang et al., 2015).

previous results obtained from nanoindentation (Biener et al., 2005; Biener et al., 2006; Hodge et al., 2007) or micropillar compression (Volkert et al., 2006). Jin et al. explained this inconsistency in (Jin et al., 2009) as result of the derivation of the yield strength from the indentation hardness via $H = \sigma_y$. It was found that the conventional relationship for a massive material of $H = 3\sigma_y$ is in better agreement to the experimental data. As shown in (Lührs et al., 2016) there exists a plastic Poisson's ratio unequal to zero, meaning that the relation $H = \sigma_y$ is not justified, because it can be only assumed on fully compressible materials (Jin et al., 2009).

5. Conclusions

In this work, the recently proposed model for nanoporous gold in (Huber et al., 2014) was extended. With respect to the effects of the chosen boundary conditions, an improved RVE with well-defined boundaries and increased density owing to the randomization of an ordered diamond cubic structure was developed. It was found, that the deviation between symmetric and periodic boundary conditions is 10% and 20% in the macroscopic yield strength and Young's modulus, respectively. Considering that the relevant literature typically discusses the results for the yield strength versus ligament size in log–log diagrams, this accuracy is sufficient compared to other uncertainties. However, the increased density, as a result of distorted ligaments, has a significant influence for randomization amplitudes greater than $A > 0.16$.

If this effect is not incorporated in the scaling equations, the errors in the determined Young's modulus and yield strength are up to a factor of 2.5.

To make a precise calculation of the solid fraction within the RVE possible, a new way of generating a RVE was presented, providing well-defined planes and edges, independent of the ligaments' random distortion. To this end, the RVE has been cut out of a much larger distorted structure. The few remaining segments of free floating ligaments were eliminated from the finite element model without loss of accuracy. The increased total ligament length due to the structural distortion was computed for 10 realizations and varying randomization parameter A. The result is an additional dependency of A in the calculated solid fraction - thus, an extension of the scaling laws, proposed in (Huber et al., 2014). To remain consistent, all data for yield strength and Young's modulus were recalculated with the new RVE and are presented in form of modified scaling equations for the relevant range of solid fractions. In addition, the dependency of the elastic Poisson's ratio was determined as function of A.

With this knowledge materials could in principle be designed with respect to the desired stiffness, Poisson's ratio, and strength by generating a microstructure with a defined randomization, e.g. by using additive manufacturing similar to (Jang et al., 2013; Zheng et al. 2014), where this is done for periodic structures. For materials that are produced in larger volumes, such as open cell foams or nanoporous gold, the degree of randomization is typically defined by the physics behind manufacturing process. In this case it is preferable to control the solid fraction and the length scale of the structural features to achieve the desired macroscopic properties and to determine the randomization of the microstructure as result of the process.

It was found, that the elastic Poisson's ratio provides a much more robust basis for the calibration of A than the Young's modulus. Based on experimental data from recent literature, A was determined to a value of 0.23, which is roughly half of the value determined in (Huber et al., 2014). The recalculation based on this value leads to a corrected yield strength of $\sigma_{ys} \approx 180$ MPa for the related ligament size of 63 nm (Huber et al., 2014). Analyzing additional data from literature, the size effect of the yield strength was investigated and compared to independently obtained values from compression tests of polymer infiltrated nanoporous gold (Wang et al., 2015). It could be shown that the determined yield strength is in excellent agreement with the experimental results.

In conclusion, three different approaches for the determination of the yield strength of nanoporous gold were compared. One approach presented in (Jin et al., 2009) is based on indentation hardness. The approach, presented in (Wang et al., 2015), makes use of the known strength of a polymer in a composite material. The yield strength of the metal phase is determined as difference between the macroscopic strength of the composite and the polymer phase. The third approach, presented in this work, is based on scaling laws applied to compression tests on nanoporous gold samples. Combining these three methods, the validity and applicability of the approaches was demonstrated.

Acknowledgments

Support by Deutsche Forschungsgemeinschaft within SFB 986 "M^3", project B4, data from compression tests of nanoporous gold provided by L. Lührs and K. Wang and the valuable discussions with J. Weissmüller, SFB 986 "M^3", project B2 are gratefully acknowledged.

References

Balk, T.J., Eberl, C., Sun, Y., Hemker, K., Gianola, D., 2009. Tensile and compressive microspecimen testing of bulk nanoporous gold. JOM 61 (12), 26–31.
Biener, J., Hodge, A.M., Hamza, A.V., Hsiung, L.M., Satcher, J.H., 2005. Nanoporous Au: a high yield strength material. J. Appl. Phys. 97 (2), 024301.
Biener, J., Hodge, A.M., Hayes, J.R., Volkert, C.A., et al., 2006. Size effects on the mechanical behavior of nanoporous Au. Nano Lett. 6 (10), 2379–2382.
Biener, J., Wittstock, A., Zepeda-Ruiz, L.A., Biener, M.M., et al., 2009. Surface-chemistry-driven actuation in nanoporous gold. Nat. Mater. 8 (1), 47–51.
Chen, L.Y., Fujita, T., Chen, M.W., 2012. Biofunctionalized nanoporous gold for electrochemical biosensors. Electrochim. Acta 67, 1–5.
Dassault Systèmes, 2014. Abaqus 6.14 Documentation.
Ding, Y., Chen, M., 2009. Nanoporous metals for catalytic and optical applications. MRS Bull. 34 (08), 569–576.
Erlebacher, J., Aziz, M.J., Karma, A., Dimitrov, N., Sieradzki, K., 2001. Evolution of nanoporosity in dealloying. Nature 410 (6827), 450–453.
Farkas, D., Caro, A., Bringa, E., Crowson, D., 2013. Mechanical response of nanoporous gold. Acta Mater. 61 (9), 3249–3256.
Gibson, L.J., Ashby, M.F., 1997. Cellular Solids: Structure and Properties. Cambridge university press.
Greer, J.R., Oliver, W.C., Nix, W.D., 2005. Size dependence of mechanical properties of gold at the micron scale in the absence of strain gradients. Acta Mater. 53 (6), 1821–1830.
Hakamada, M., Mabuchi, M., 2007. Mechanical strength of nanoporous gold fabricated by dealloying. Scr. Mater. 56 (11), 1003–1006.
Hodge, A.M., Biener, J., Hayes, J.R., Bythrow, P.M., et al., 2007. Scaling equation for yield strength of nanoporous open-cell foams. Acta Mater. 55 (4), 1343–1349.
Huber, N., Viswanath, R.N., Mameka, N., Markmann, J., Weissmüller, J., 2014. Scaling laws of nanoporous metals under uniaxial compression. Acta Mater. 67, 252–265.
Jang, D., Meza, L.R., Greer, F., Greer, J.R., 2013. Fabrication and deformation of three-dimensional hollow ceramic nanostructures. Nat. Mater. 12, 893–898.
Jin, H.-J., Kurmanaeva, L., Schmauch, J., Rösner, H., et al., 2009. Deforming nanoporous metal: Role of lattice coherency. Acta Mater. 57 (9), 2665–2672.
Kramer, D., Viswanath, R.N., Weissmüller, J., 2004. Surface-stress induced macroscopic bending of nanoporous gold cantilevers. Nano Lett. 4 (5), 793–796.
Li, R., Sieradzki, K., 1992. Ductile-brittle transition in random porous Au. Phys. Rev. Lett. 68 (8), 1168–1171.
Lührs, L., Soyarslan, C., Markmann, J., Bargmann, S., Weissmüller, J., 2016. Elastic and plastic Poisson's ratio of nanoporous gold. Scr. Mater. 110, 65–69.
Mameka, N., Markmann, J., Jin, H.-J., Weissmüller, J., 2014. Electrical stiffness modulation-confirming the impact of surface excess elasticity on the mechanics of nanomaterials. Acta Mater. 76, 272–280.

Ngô, B.-N.D., Stukowski, A., Mameka, N., Markmann, J., et al., 2015. Anomalous compliance and early yielding of nanoporous gold. Acta Mater. 93, 144–155.
Parida, S., Kramer, D., Volkert, C.A., Rösner, H., et al., 2006. Volume change during the formation of nanoporous gold by dealloying. Phys. Rev. Lett. 97 (3), 35504.
Pia, G., Delogu, F., 2015a. A phenomenological approach to yield strength in nanoporous metal foams. Scr. Mater. 103, 26–29.
Pia, G., Delogu, F., 2015b. Nanoporous Au: statistical analysis of morphological features and evaluation of their influence on the elastic deformation behavior by phenomenological modeling. Acta Mater. 85, 250–260.
Roberts, A.P., Garboczi, E.J., 2002. Elastic properties of model random three-dimensional open-cell solids. J. Mech. Phys. Solids 50 (1), 33–55.
Snyder, J., Fujita, T., Chen, M.W., Erlebacher, J., 2010. Oxygen reduction in nanoporous metal–ionic liquid composite electrocatalysts. Nat. Mater. 9 (11), 904–907.
Sun, S., Chen, X., Badwe, N., Sieradzki, K., 2015. Potential-dependent dynamic fracture of nanoporous gold. Nat. Mater. 14 (9), 894–898.
Sun, X.-Y., Xu, G.-K., Li, X., Feng, X.-Q., Gao, H., 2013. Mechanical properties and scaling laws of nanoporous gold. J. Appl. Phys. 113 (2), 023505.
Uchic, M.D., Dimiduk, D.M., Florando, J.N., Nix, W.D., 2004. Sample dimensions influence strength and crystal plasticity. Science 305 (5686), 986–989.
Volkert, C.A., Lilleodden, E.T., 2006. Size effects in the deformation of sub-micron Au columns. Philos. Mag. 86 (33–35), 5567–5579.
Volkert, C.A., Lilleodden, E.T., Kramer, D., Weissmüller, J., 2006. Approaching the theoretical strength in nanoporous Au. Appl. Phys. Lett. 89 (6), 061920.
Wang, K., Kobler, A., Kubel, C., Jelitto, H., et al., 2015. Nanoporous-gold-based composites: toward tensile ductility. NPG Asia Mater. 7, e187.
Wang, K., Weissmüller, J., 2013. Composites of nanoporous gold and polymer. Adv. Mater. 25 (9), 1280–1284.
Wang, L.C., Zhong, Y., Widmann, D., Weissmueller, J., Behm, R.J., 2012. On the role of residual Ag in nanoporous Au catalysts for CO oxidation: a combined microreactor and TAP reactor study. ChemCatChem 4 (2), 251–259.
Weissmüller, J., Newman, R.C., Jin, H.-J., Hodge, A.M., Kysar, J.W., 2009. Nanoporous metals by alloy corrosion: formation and mechanical properties. MRS Bull. 34 (08), 577–586.
Wu, B., Heidelberg, A., Boland, J.J., 2005. Mechanical properties of ultrahigh-strength gold nanowires. Nat. Mater. 4 (7), 525–529.
Yang, F., Li, J.C.-M., 2008. Micro and Nano Mechanical Testing of Materials and Devices. Springer.
Zheng, X., Lee, H., Weisgraber, T.H., Shusteff, M., et al., 2014. Ultralight, ultrastiff mechanical metamaterials. Science 344 (6190), 1373–1377.
Zhu, H.X., Hobdell, J.R., Windle, A.H., 2000. Effects of cell irregularity on the elastic properties of open-cell foams. Acta Mater. 48 (20), 4893–4900.